

A high-order, conservative and positivity-preserving intersection-based remapping method between meshes with isoparametric curvilinear cells

Nuo Lei^{1 2}, Juan Cheng³ and Chi-Wang Shu⁴

Abstract

This paper presents a novel intersection-based remapping method for isoparametric curvilinear meshes within the indirect arbitrary Lagrangian-Eulerian (ALE) framework, addressing the challenges of transferring physical quantities between high-order curved-edge meshes. Our method leverages the Weiler-Atherton clipping algorithm to compute intersections between curved-edge quadrangles, enabling robust handling of arbitrary order isoparametric curves. By integrating multi-resolution weighted essentially non-oscillatory (WENO) reconstruction, we achieve high-order accuracy while suppressing numerical oscillations near discontinuities. A positivity-preserving limiter is further applied to ensure physical quantities such as density remain non-negative without compromising conservation or accuracy. Notably, the computational cost of handling higher-order curved meshes, such as cubic or even higher-degree parametric curves, does not significantly increase compared to second-order curved meshes. This ensures that our method remains efficient and scalable, making it applicable to arbitrary high-order isoparametric curvilinear cells without compromising performance. Numerical experiments demonstrate that the proposed method achieves high-order accuracy, strict conservation (with errors approaching machine precision), essential non-oscillation and positivity-preserving.

Keywords: Isoparametric meshes; Data transfer; Remapping; High-order accuracy; Conservative; Positivity-preserving.

¹Hua Loo-Keng Center for Mathematical Sciences, Academy of Mathematics and Systems Science, Chinese Academy of Sciences, Beijing, 100190, China. E-mail: nuo_lei@lsec.cc.ac.cn. Research is supported in part by NSFC grant 12288201.

²Department of Applied Mathematics, The Hong Kong Polytechnic University, Hung Hom, Kowloon, Hong Kong. Research is supported in part by the 2024 Hong Kong Scholar Program G-YZ7Q.

³Academy for Multidisciplinary Studies, Capital Normal University, Beijing 100048, China. E-mail: jcheng@cnu.edu.cn. Research is supported in part by NSFC grant 12031001 and National Key R&D Program of China No. 2023YFA1009003.

⁴Division of Applied Mathematics, Brown University, Providence, RI 02912, USA. E-mail: chi-wang.shu@brown.edu. Research is supported in part by NSF grant DMS-2309249.

1 Introduction

The arbitrary Lagrangian-Eulerian (ALE) method is a powerful framework for computational fluid dynamics, particularly for moving boundary and multi-material problems. The indirect ALE method combines the strengths of the Lagrangian and Eulerian descriptions and comprises three key components: First, the Lagrangian phase, where the mesh moves in conjunction with the fluid flow to solve the fluid dynamics equations. Second, the rezoning (remeshing) phase, which is performed to enhance mesh quality. Last, the remapping phase, which involves transferring physical variables from the original mesh to the newly rezoned mesh. In [6], the authors pointed out that for a Lagrangian scheme in 2D, it can be at most second-order accurate if curved meshes are not used. These limitations have spurred the development of curvilinear Lagrangian schemes and ALE methods [7, 9, 2, 20, 17], which employ higher-order curved elements to achieve superior geometric representation, enhancing numerical accuracy, and robustness under large deformations.

Nevertheless, the increased geometric complexity of curvilinear meshes introduces substantial challenges, particularly during the remapping phase. Robust remapping techniques must preserve critical properties such as conservation, high-order accuracy, and positivity. Overcoming these challenges is essential for advancing the capabilities of curvilinear ALE methods. While there has been considerable research and notable progress in developing remapping methods for straight-line meshes, the adaptation of these methods to curvilinear meshes has been relatively under-explored.

The advection-based remapping method [11, 1, 14] is a popular approach, which solves a transport equation over a pseudo-time interval to simulate the advection of physical quantities from a source mesh to a target mesh. Based on the theory of virtual element projectors, Lipnikov and his collaborators [21, 22] have developed high-order conservative advection-based remapping method for curvilinear meshes. This approach ensures that the remapping process preserves important physical properties and maintains the overall accuracy of the simulation.

The flux-based (or swept-based) remapping method [10, 24, 16] leverages the divergence theorem to convert the area integral over the swept region into a line integral along cell boundaries, thereby computing the fluxes of physical quantities across interfaces and updating the values on the target mesh. In recent years, the authors in [23] have extended the swept-based remapping method to more general curved polygonal meshes, developing conservative and bound-preserving method.

The advection-based and flux-based approaches are highly efficient for structured meshes with consistent topology and small mesh motions. However, they are not suitable for scenarios involving large mesh movements or changes in the topological connectivity of the mesh.

The intersection-based remapping method [12, 15, 27], which computes the overlappings between old and new cells, offers inherent conservation properties and can handle arbitrary mesh motions. Due to their flexibility, these methods are particularly attractive for remeshing problems where the topology may differ. A wide range of intersection-based remapping methods have been developed, spanning from two-dimensional to three-dimensional cases [26, 18, 19], from low-order to high-order methods, and including bound-preserving properties [3, 16, 24].

These methods, primarily designed for straight-edge meshes, face significant challenges when applied to curved-edge meshes. The complexity of geometric intersections and the computational cost of solving high-order polynomial equations make accurate intersection calculations difficult. Maintaining numerical precision and consistency is crucial to ensure conservation and avoid distortions in the remapped fields. These challenges underscore the need for advanced algorithms that can efficiently handle curved meshes while preserving essential physical properties and avoiding numerical oscillations.

In a notable advancement, the authors in [27] proposed the first intersection-based remapping method for second-order isoparametric curvilinear meshes. They divided the isoparametric curvilinear cell into several sub-cells and identified intersections using a set-based

method, which is limited to second-order curves. Nevertheless, this approach cannot handle higher-order curves and therefore cannot be extended to higher-order ALE curved mesh methods, which significantly limits its applicability.

In this paper, we introduce a novel two-dimensional intersection-based remapping method tailored for curvilinear meshes. Our approach is capable of handling arbitrary high-order parameterized curves, thereby enabling precise representation of complex geometries. By applying high-order multi-resolution WENO reconstruction, our method achieves high-order accuracy while ensuring strict conservation and essentially non-oscillatory properties. Additionally, the application of a positivity-preserving limiter ensures that positivity is maintained without compromising high-order accuracy. This work represents a significant advancement in curvilinear ALE methods, offering a reliable and efficient tool for high-fidelity simulations in computational fluid dynamics.

We incorporate the Weiler-Atherton (WA) clipping algorithm, a well-established method in computer graphics, to address intersection-based remapping for curvilinear meshes. The WA algorithm efficiently computes intersection points and generates accurate boundaries at a relatively low computational cost, making it suitable for complex geometries. Its ability to handle both convex and concave polygons ensures versatility in geometric operations, crucial for dealing with the intricate shapes of curved-edge elements. This marks the first application of the WA algorithm to intersection-based remapping, demonstrating its effectiveness and rationality in this context. Our approach inherits the flexibility of intersection-based methods, allowing for large mesh deformations and remeshing without requiring identical mesh connectivity or topology. Compared to previous approaches [27], our method naturally extends to higher-order curvilinear meshes without significant computational overhead, enhancing its applicability and efficiency.

We consider solving fluid dynamics in a cell-centered finite volume framework, where the cell averages of each cell are known. To achieve high-order accuracy in the remapping procedure, we employ the multi-resolution weighted essentially non-oscillatory (WENO) recon-

struction approach [31]. This method utilizes hierarchical central spatial stencils to achieve optimal accuracy in smooth regions while effectively suppressing oscillations near discontinuities, with the added flexibility of arbitrary positive linear weights summing to one. By integrating high-order WENO reconstruction into our framework, we aim to achieve both high-order accuracy and essentially non-oscillatory behavior in handling complex situations with curvilinear meshes.

The ALE method for solving CFD problems typically involves numerous non-negative physical quantities, such as density and internal energy. Preserving the positivity of these quantities throughout the simulation is therefore crucial. Many bound-preserving or positivity-preserving remapping methods have been developed to address this issue, including those based on MOOD limiters [4] or slope limiters [5]. Building on our previous studies [18, 19], we extend a positivity-preserving modification [30] to the high-order reconstructed polynomials on curvilinear meshes. This ensures that the remapped results remain positive while maintaining both conservation property and high-order accuracy.

This article begins by introducing the setup of curvilinear meshes and outlining the overall framework of our remapping method. Subsequently, from Section 3 to Section 6, we systematically elaborate on the key components of our remapping method, including high-order WENO reconstruction, the Weiler-Atherton clipping algorithm, two types of high-order numerical integrals on curved intersections, and the positivity-preserving modification. Finally, in Section 7, we present numerical experiments that demonstrate the properties of high-order accuracy, essentially non-oscillatory behavior, conservation and positivity-preserving of our remapping approach. This comprehensive development and validation process highlights the robustness of our proposed method for applications involving curvilinear meshes.

2 Basic concepts

Suppose the two-dimensional computational domain Ω is a connected domain decomposed into isoparametric elements $\mathcal{M} = \{I_i\}_{i=1}^N$ called “curvilinear quadrangles”. Each second-

order curvilinear quadrangle has four vertices and four control points on the edge. For example, consider a curved-edge with two vertex coordinates $P_1(x_{P_1}, y_{P_1})$ and $P_2(x_{P_2}, y_{P_2})$, and a control point $P_5(x_{P_5}, y_{P_5})$. We construct a quadratic curve as:

$$\begin{cases} x(t) = x_{P_1}(1 - 2t)(1 - t) + 4x_{P_5}t(1 - t) + x_{P_2}(2t - 1)t, \\ y(t) = y_{P_1}(1 - 2t)(1 - t) + 4y_{P_5}t(1 - t) + y_{P_2}(2t - 1)t, \end{cases}$$

where $t \in [0, 1]$. This curve is designed such that it passes through P_1 , P_5 , and P_2 at $t = 0$, $t = 0.5$, and $t = 1$, respectively. Similarly, each third-order curvilinear quadrangle has four vertices and eight control points on the edge. Figure 2.1 shows some examples for the second-order and third-order curvilinear quadrangles.

For the curvilinear mesh \mathcal{M} , we have some basic requirements:

- There are neither overlaps nor gaps between any two neighboring cells,

$$\bigcup_{i=1}^N I_i = \Omega, \quad |I_i \cap I_j| = 0 \quad \forall i \neq j.$$

- All of the cells $\{I_i\}_{i=1}^N$ should not be self-intersecting.
- All of the cells $\{I_i\}_{i=1}^N$ do not have holes.

Obviously, these requirements are natural and we also require the new rezoned mesh $\widetilde{\mathcal{M}} = \{\widetilde{I}_{\tilde{i}}\}_{\tilde{i}=1}^{\tilde{N}}$ satisfies them. We denote the intersection of the old cell I_i and the new cell $\widetilde{I}_{\tilde{i}}$ as $\hat{I}_{i,\tilde{i}} := I_i \cap \widetilde{I}_{\tilde{i}}$.

In this work, we focus on remapping cell averages from \mathcal{M} to $\widetilde{\mathcal{M}}$. Suppose we have cell averages \bar{u}_i in each cell I_i , then we need to calculate the new cell average $\bar{\tilde{u}}_{\tilde{i}}$ in $\widetilde{I}_{\tilde{i}}$ for $\tilde{i} = 1, \dots, \tilde{N}$. Refer to our previous work [18], the flowchart of our curved remapping method follows as,

1. **High-order reconstruction:** Reconstruct high-order polynomial $u_i(x, y)$ in each old cell I_i with the multi-resolution WENO idea.
2. **Weiler-Atherton clipping:** Find the intersection $\hat{I}_{i,\tilde{i}}$ between each old and new isoparametric cells.

3. **The Positivity-preserving modification:** Modify $u_i(x, y)$ by the positivity-preserving limiter to maintain positivity for the physically positive variables, denote the resulting modified polynomial as $\hat{u}_i(x, y)$.
4. **Numerical integration:** Calculate the integration for the modified polynomials over the intersections $\int_{\hat{I}_{i,\tilde{i}}} \hat{u}_i(x, y) dx dy$.

Finally, we can calculate the new cell averages as

$$\bar{u}_{\tilde{i}} := \frac{1}{|\tilde{I}_{\tilde{i}}|} \sum_{i=1}^N \int_{\hat{I}_{i,\tilde{i}}} \hat{u}_i(x, y) dx dy.$$

Based on clipping the intersection exactly and high-order quadrature rule, we can prove that this curved remapping method is conservative, see [18] for the detailed proof. Next, we will present a step-by-step explanation of our remapping method.

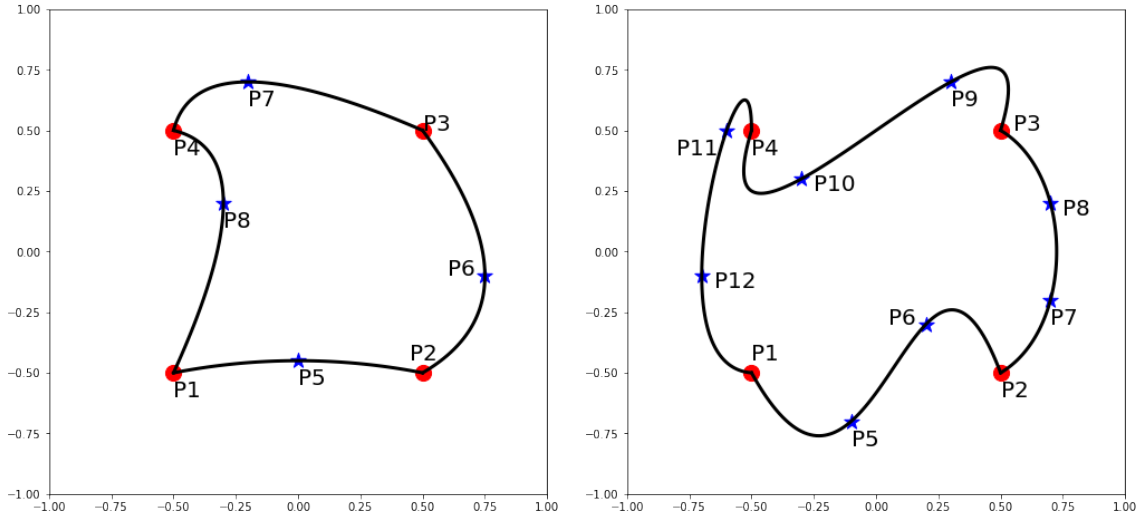


Figure 2.1: The second-order and third-order isoparametric cells. Red markers are vertices and blue markers are control points.

3 High-order reconstruction

On the original curvilinear mesh \mathcal{M} , we employ the multi-resolution WENO approach [31] to reconstruct high-order and conservative polynomials $\{u_i(x, y)\}_{i=1}^N$. For illustration, we

focus on the third-order WENO reconstruction. This method can be naturally extended to higher orders by increasing the number of stencils and polynomial degrees while maintaining the essential properties of the reconstruction.

1. Select a small stencil $S_0 = \{I_i\}$ and a big stencil $S_1 = \{I_j | I_j \cap I_i \neq \emptyset\}$. Here, we consider curved quadrilateral cells. Thus, the big central stencil S_1 includes the cell I_i itself, four cells sharing edges with I_i , and four cells sharing vertices with I_i . It can also be seen that S_0 is contained within S_1 , $S_0 \subset S_1$.
2. Reconstruct a zeroth-degree polynomial $q_0(x, y) = \bar{u}_i$ on S_0 and reconstruct quadratic polynomial $q_1(x, y) \in \mathbb{P}^2(I_i)$ on S_1 such that

$$\begin{aligned} q_1(x, y) &= \arg \min_{\tilde{q}_1 \in \mathbb{P}^2} \sum_{I \in S_1} \left| \iint_I \tilde{q}_1(x, y) dx dy - \bar{u}_I |I| \right|^2, \\ \text{s.t. } &\iint_{I_i} \tilde{q}_1(x, y) dx dy = \bar{u}_i |I_i|. \end{aligned} \quad (3.1)$$

where $|I|, |I_i|$ are the area of the relative cells.

3. Take $p_0(x, y) = q_0(x, y)$ and $p_1(x, y) = \frac{1}{\gamma_1} q_1(x, y) - \frac{\gamma_0}{\gamma_1} p_0(x, y)$, with linear weights $\gamma_0 + \gamma_1 = 1$ and $\gamma_0, \gamma_1 > 0$. Following [31], we choose $\gamma_0 = \frac{1}{101}$ and $\gamma_1 = \frac{100}{101}$.
4. Define the smoothness indicators as

$$\beta_1 := \sum_{l_1+l_2=1,2} \iint_{I_i} |I_i|^{l_1+l_2-1} \left(\frac{\partial^{l_1+l_2}}{\partial x^{l_1} \partial y^{l_2}} p_1(x, y) \right)^2 dx dy, \quad l_1, l_2 = 0, 1, 2, \quad (3.2)$$

and $\beta_0 = \min_{I_j \in S_1 \setminus \{I_i\}} \{(\bar{u}_i - \bar{u}_j)^2\}$, where the designed smoothness indicators β_0, β_1 can avoid the numerical oscillation near the discontinuity.

5. Define the nonlinear weights as

$$\omega_0 = \frac{\bar{\omega}_0}{\bar{\omega}_0 + \bar{\omega}_1}, \quad \omega_1 = \frac{\bar{\omega}_1}{\bar{\omega}_0 + \bar{\omega}_1}, \quad \text{with } \bar{\omega}_l = \gamma_l \left(1 + \frac{\tau}{\beta_l + \epsilon} \right), \quad l = 0, 1,$$

where $\tau = \frac{|\beta_0 - \beta_1|^2}{4}$ and $\epsilon = 10^{-4}$.

6. Finally, the reconstructed polynomial is

$$u_i(x, y) := \omega_0 p_0(x, y) + \omega_1 p_1(x, y).$$

Notice that, in (3.1) and (3.2), the integrals of polynomials over curved cells are needed. We use Green's theorem to transform the integral over the curved cells into a line integral, and then apply one-dimensional high-order integration formulas for its computation. For example, ∂I_i has four segments $\{L_l\}_{l=1}^4$ and each segment L_l is parameterized by the expressions $x = x_l(t), y = y_l(t)$ for $t \in [0, 1]$. Then, we have,

$$\begin{aligned} \iint_{I_i} f(x, y) dx dy &= \int_{\partial I_i} f_1(x, y) dx + f_2(x, y) dy \\ &= \sum_{l=1}^4 \int_0^1 (f_1(x_l(t), y_l(t)) x'_l(t) + f_2(x_l(t), y_l(t)) y'_l(t)) dt \end{aligned} \tag{3.3}$$

where $f(x, y)$ is the basis polynomial integrand and polynomials $f_1(x, y), f_2(x, y)$ satisfy $\frac{\partial f_2}{\partial x} - \frac{\partial f_1}{\partial y} = f$.

In the multi-resolution WENO approach, the positive linear weights are flexible, and fewer high-order reconstructions are required, making the method significantly more efficient than the classical WENO approach. In the procedure, we reconstruct a high-order polynomial and a low-order polynomial on the central nested stencils, with nonlinear weights assigned based on their smoothness. This reconstruction ensures that the resulting polynomial retains high-order accuracy in smooth regions while placing greater emphasis on low-order polynomials near discontinuities, effectively suppressing numerical oscillations and improving algorithm stability.

4 The Weiler-Atherton clipping algorithm

The Weiler-Atherton (WA) clipping algorithm [29] is a robust computational geometry technique for clipping polygons. Unlike the simpler methods such as the Sutherland-Hodgman algorithm [28], which are limited to convex polygons and straight-edge meshes, the WA al-

gorithm supports both convex and concave polygons, making it highly versatile for isoparametric curved meshes. It works by identifying intersection points between the subject and clipping polygons, then traversing their boundaries to construct the clipped result to ensure accurate traversal order. The flowchart of the WA clipping algorithm follows as,

1. **Intersection points detection and labeling:** First, we calculate all intersection points between the curved edges. Each intersection point is then labeled as either “entering” or “exiting” the clipping polygons, depending on the relative orientation of the two polygons. To achieve this, we use nonlinear root-finding algorithms, such as the Newton method, to solve the parametric equations between two curved edges and locate the intersection points. In our implementation, the error tolerance for the nonlinear root-finding algorithm is set to 10^{-12} .
2. **Path construction:** Once all intersection points are determined and labeled, the algorithm constructs the resultant polygon(s). This is done by traversing the subject polygon and clipping polygon alternately, starting from an “entering” intersection point and following the edges of the polygons until an “exiting” point is reached. At each intersection, the algorithm switches between the subject and clipping polygons. This ensures that only the portions of the subject polygon inside the clipping polygon are retained. The traversal continues until a closed path is formed. For complex cases, such as multiple disjoint intersections, the algorithm handles each path independently, generating multiple output polygons as needed.

A key strength of the WA algorithm is its ability to handle complex scenarios, such as multiple intersections or disjoint intersections. Notably, it is also applicable to curvilinear polygons, making it suitable for finding intersections in curved meshes. Despite these constraints, its flexibility and accuracy make it a valuable tool in computer graphics, CAD systems, and GIS for complex geometric operations.

Following [27], we consider two cells “Quad P” and “Quad Q” in Table 4.1, and each of

the curves is a quadratic curve. Specifically, we consider using this example to illustrate our WA algorithm.

Step 1: Define the contours for the two quadrilaterals in a counterclockwise order $P_1 \rightarrow P_2 \rightarrow P_3 \rightarrow P_4 \rightarrow P_1$, $Q_1 \rightarrow Q_2 \rightarrow Q_3 \rightarrow Q_4 \rightarrow Q_1$. Based on the vertices and control points, we derive the parametric expressions $\{x_l^P(t), y_l^P(t)\}_{l=1}^4$ for “Quad P” with $t \in [0, 1]$ and $\{x_l^Q(s), y_l^Q(s)\}_{l=1}^4$ for “Quad Q” with $s \in [0, 1]$.

Step 2: Compute the intersections of the curves pairwise, using the Newton method to solve the nonlinear equations

$$\begin{cases} x_{l_1}^P(t) = x_{l_2}^Q(s) \\ y_{l_1}^P(t) = y_{l_2}^Q(s) \end{cases} \quad \text{with } t, s \in [0, 1] \quad \forall 1 \leq l_1, l_2 \leq 4,$$

to obtain the coordinates of intersection points. Then, label the entry or exit of the intersection according to the connecting order of the contours, as shown in Table 4.2.

Step 3: Place the intersection points in sequential order into our linked lists, resulting in two new linked lists, as shown on the left side of Figure 4.1.

Step 4: Start from the entry point of the subject polygon and traverse along the linked list. If an exit point is encountered, switch to the clipping polygon. Continue traversing along the linked list of the clipping polygon, and if an entry point is encountered, switch back to the subject polygon. This process of switching between the two linked lists continues until a closed loop is formed. Since there may be multiple intersections, repeat this path selection process until all intersection points have been utilized. See the right side of Figure 4.1 for the two closed loops.

In Figure 4.2, we mark the two cells in black and red lines, and mark the intersections in blue solid lines. Moreover, in practical applications, careful handling of various degenerate cases is necessary, such as point-to-point, point-to-edge, and edge-to-edge coincidences. In Figure 4.3, we present several examples of the WA algorithm under extreme conditions, demonstrating its robustness.

Remark 4.1. *It can be seen from the above flowchart that the WA clipping algorithm can be easily extended to higher-order curved meshes or other types of curved grids without a significant increase in computational cost. For example, we demonstrate the computational results for third-order curved meshes in Figure 4.4.*

Table 4.1: Example quadratic cells.

Quad P			Quad Q		
	x	y		x	y
P_1	-1.5	-2	Q_1	-1	-2
P_2	1	-1	Q_2	1	-2
P_3	1	1	Q_3	1	0.1
P_4	-1	1	Q_4	-0.875	0.2
P_5	0.1	-0.1	Q_5	-0.7	-0.55
P_6	1.4	0	Q_6	1.4	-1
P_7	0	0.9	Q_7	0	-0.25
P_8	-0.8	0	Q_8	-1.4	-1

Table 4.2: Coordinates of the intersection points of Quad A and Quad B in Table 4.1.

Intersection points							
	x	y	type		x	y	type
'1'	-1.05713663	-1.29598616	exit	'2'	-0.51624632	-0.58935822	entry
'3'	-0.13487741	-0.23429411	exit	'4'	0.57041875	-0.14211494	entry
'5'	-1.27097304	-1.62405364	entry	'6'	1.30701824	-0.48213526	exit
'7'	-0.78370680	0.11026931	entry	'8'	-1.30299176	-1.55541394	exit

5 Numerical integration over curvilinear intersection

After clipping between curved cells, we next address the computation of high-order polynomial integrals over the resulting intersections. In [18], where the intersections are standard polygons, they are subdivided into multiple triangles by connecting vertices, and a high-order quadrature rule is applied to evaluate the integrals. However, this method is not directly applicable to curved-edge polygons. When connecting two vertices with a straight line, it may intersect other curved edges, resulting in an incorrect partitioning. To accurately compute

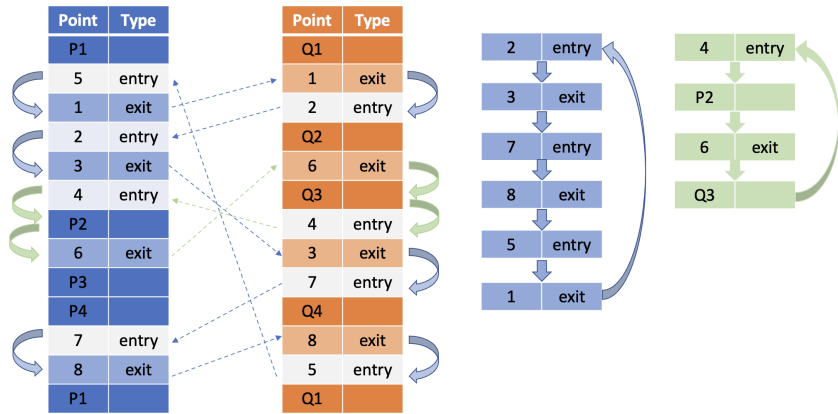


Figure 4.1: Linked list example.

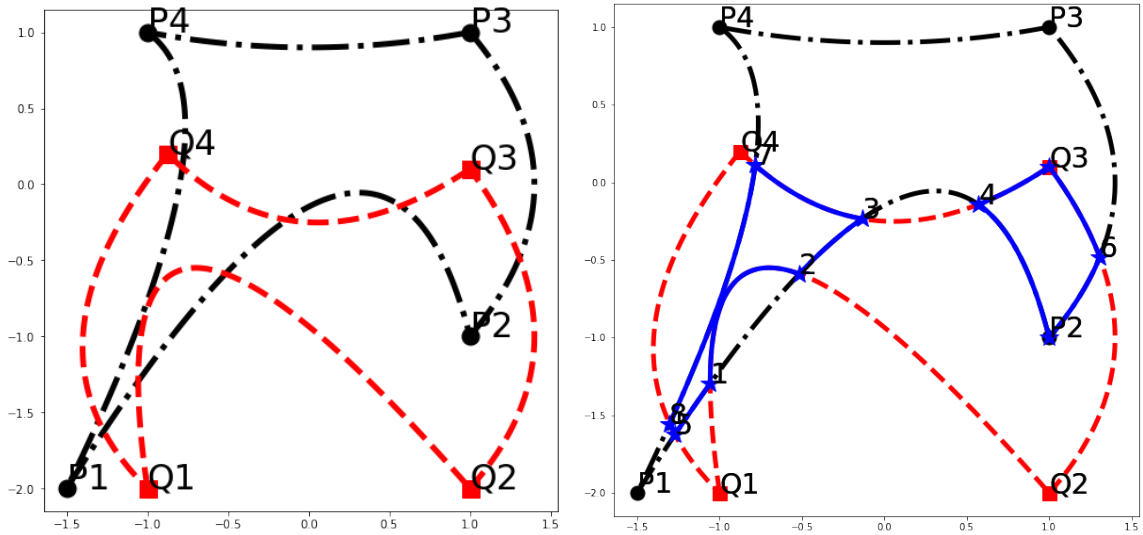


Figure 4.2: Clipping example with the WA algorithm.

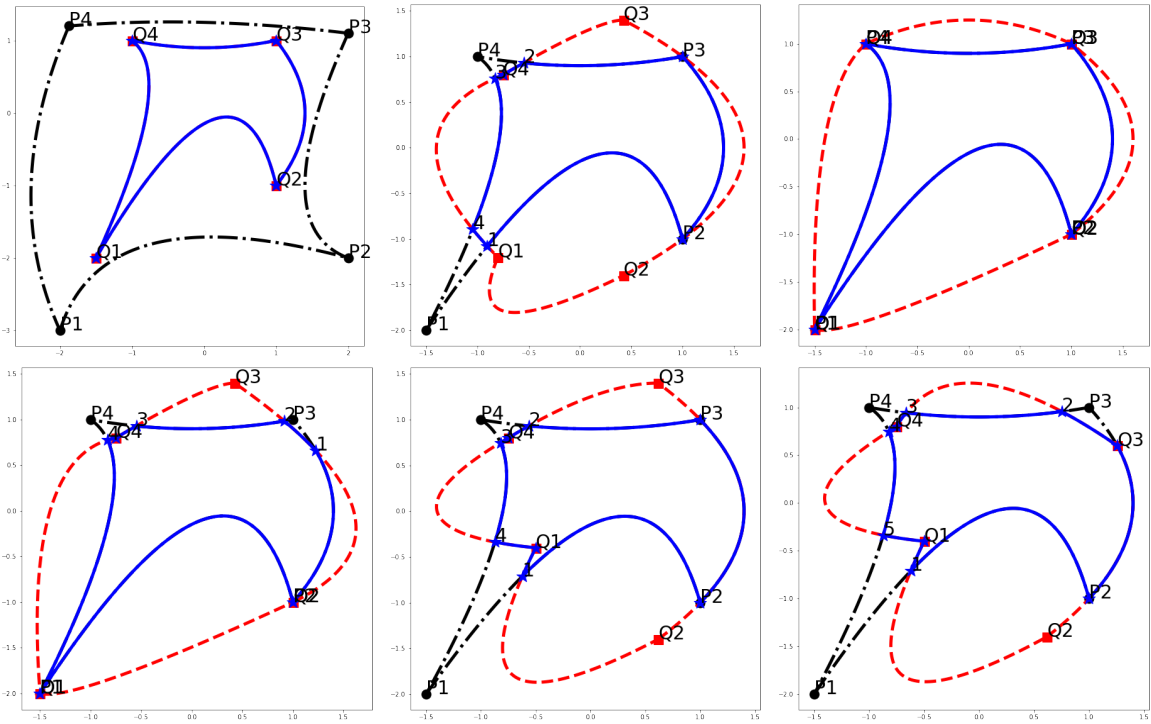


Figure 4.3: Some degenerate cases with the WA clipping algorithm.

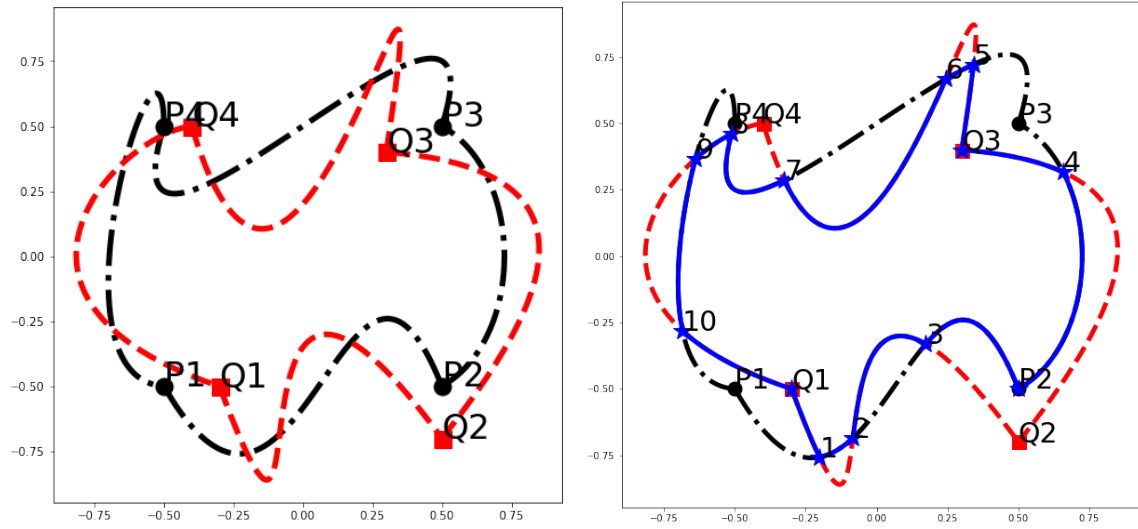


Figure 4.4: Clipping example with the WA algorithm for third-order isoparametric cells.

the integral of a polynomial over the intersection of curved-edge polygons, in this section, we will propose two approaches.

First, we transform the two-dimensional integral into a one-dimensional contour integral along the curved boundaries, which has been mentioned in (3.3). Specifically, assume the edge of the intersection $\partial\hat{I}_{i,\tilde{i}}$ has S segments $\{L_l\}_{l=1}^S$ with expressions $x = x_l(t), y = y_l(t)$ for $t \in [t_l^{\text{sta}}, t_l^{\text{end}}]$ and $l = 1, \dots, S$. Notice that, since each edge of the intersection lies either on ∂I_i or $\partial\tilde{I}_{\tilde{i}}$, the expressions $(x_l(t), y_l(t))$ are known, and the parameters $t_l^{\text{sta}}, t_l^{\text{end}}$ are already computed during the WA clipping algorithm. This ensures that all necessary geometric information is readily available for further calculations. Then, we use Green's theorem such that,

$$\iint_{\hat{I}_{i,\tilde{i}}} f(x, y) dx dy = \sum_{l=1}^S \int_{t_l^{\text{sta}}}^{t_l^{\text{end}}} (f_1(x_l(t), y_l(t))x'_l(t) + f_2(x_l(t), y_l(t))y'_l(t)) dt \quad (5.1)$$

where $f(x, y)$ is the polynomial integrand and polynomials $f_1(x, y), f_2(x, y)$ satisfy $\frac{\partial f_2}{\partial x} - \frac{\partial f_1}{\partial y} = f$. Setting $f = 1$, we could compute the area of the curved-edge intersection using the following formula:

$$|\hat{I}_{i,\tilde{i}}| = \iint_{\hat{I}_{i,\tilde{i}}} 1 dx dy = \frac{1}{2} \int_{t_l^{\text{sta}}}^{t_l^{\text{end}}} (x_l(t)y'_l(t) - y_l(t)x'_l(t)) dt.$$

The second approach involves partitioning the curved-edge polygons into multiple small curved-edge triangles and applying high-order quadrature rules for integration. As previously mentioned, when the intersection involves curved-edge polygons, directly decomposing the intersection into small triangles to locate all integration points becomes nontrivial.

The ear-clipping algorithm [25] is a classical method for triangulating polygons and is applicable to arbitrary 2D polygons, including both convex and concave shapes. This method works by iteratively identifying and removing ‘‘ears’’ (triangles formed by three consecutive vertices that do not contain any other vertices of the polygon), ultimately decomposing the polygon into a set of non-overlapping triangles.

Therefore, we first insert a set of points $\{v_l^n\}_{l=1}^S, n \in \mathbb{N}$ along the intersection edges $\partial\hat{I}_{i,\tilde{i}}$ and employ the ear-clipping algorithm to iteratively extract small curved-edge triangles by

connecting vertices and inserting additional points $\{v_l^n\}_{l=1}^S$, thereby ensuring a complete and accurate partitioning of the intersection. If a self-intersecting curved triangle appears, we will continue to increase points until no self-intersecting curved triangle is produced.

Next, we only need to compute the integral of the polynomial over each curved-edge triangle \mathbb{T} . Note that the curved edge of \mathbb{T} must correspond to certain segments $\{L_l\}_{l=1}^S$. So, we can accurately identify the control points on each edge of \mathbb{T} . Using the three vertices and the three middle control points of \mathbb{T} , we establish a bijection $F_{\mathbb{T}} : \mathbb{T}_0 \rightarrow \mathbb{T}$, where $\mathbb{T}_0 = \{(0, 0), (0, 1), (1, 0)\}$ is the reference triangle. Assume we have the following quadrature rule on \mathbb{T}_0 ,

$$\int_{\mathbb{T}_0} f(\xi, \eta) d\xi d\eta = \sum_{m=1}^M \omega_m f(\xi_m, \eta_m),$$

where $\{\omega_m\}_{m=1}^M$ are the quadrature weights and $\{(\xi_m, \eta_m)\}_{m=1}^M$ are the quadrature points in \mathbb{T}_0 . Note that we need to require the quadrature weights be positive $\omega_m > 0$, which is very important for us to preserve positivity in the next section. Then the integral over the curved-edge triangle \mathbb{T} can be expressed as

$$\begin{aligned} \iint_{\mathbb{T}} f(x, y) dx dy &= \iint_{\mathbb{T}_0} f(F_{\mathbb{T}}(\xi, \eta)) J_{F_{\mathbb{T}}}(\xi, \eta) d\xi d\eta \\ &= \sum_{m=1}^M \omega_m f(F_{\mathbb{T}}(\xi_m, \eta_m)) J_{F_{\mathbb{T}}}(\xi_m, \eta_m) \end{aligned} \tag{5.2}$$

where $J_{F_{\mathbb{T}}}(\xi, \eta)$ is the Jacobian determinant of the mapping $F_{\mathbb{T}}$. In order to integrate a polynomial $f(x, y)$ of degree k on the curved cell \mathbb{T} exactly, we would need the quadrature rule in (5.2) on the reference cell \mathbb{T}_0 to be exact for all polynomials of degree up to $2k + 2$.

Remark 5.1. *The process of partitioning a polygonal into triangles is referred as “triangulation” in computer graphics. Evidently, the more points inserted along the curved edges, the more accurately the intersection of the curved-edge polygon can be triangulated, even though some resulting triangles may be curved-edge triangles. However, inserting too many points may reduce computational efficiency. To address this, curvature-adaptive or arc-length-adaptive inserting methods can be employed to insert points, making triangulation*

more efficient. Additionally, inserting points within the intersection can produce higher-quality triangles, as seen in methods like the Constrained Delaunay Triangulation (CDT) [8]. That said, how to efficiently triangulate is beyond the scope of this paper. Instead, we focus on ensuring that sufficient tools are available to enable the triangulation of curved-edge intersection.

For the two curved-edge polygons provided in Table 4.1, we compute the area of the intersections with two different approaches. In Table 5.1, the “exact” row denotes the exact area provided in [27], while “Approach A” and “Approach B” represent the results obtained by our edge integral method (5.1) and triangulation-based integral method (5.2), respectively. It can be observed that both of our methods exhibit extremely high precision, with integration errors close to machine zero. Figure 5.1 shows the partition of the intersection. For the intersection enclosed by third-order isoparametric cells in Figure 4.4, the results calculated using “Approach A” and “Approach B” are 1.0341187055615808 and 1.0341187055615777, respectively, which are equivalent in the sense of machine error.

Table 5.1: Area for the intersection example in Table 4.1.

	Area	Absolute error
exact	0.723 453 730 359 014 3	
Approach A	0.723 453 730 359 005 6	8.66×10^{-15}
Approach B	0.723 453 730 359 006 7	7.55×10^{-15}

Remark 5.2. *In general, using Green’s theorem to compute integrals over curved-edge polygons is much more efficient. However, this method needs to place the quadrature points along the intersection’s edge, whereas the second approach, which triangulates the intersection and applies quadrature rules, ensures that the quadrature points are distributed within the interior. This property facilitates subsequent positivity-preserving modification.*

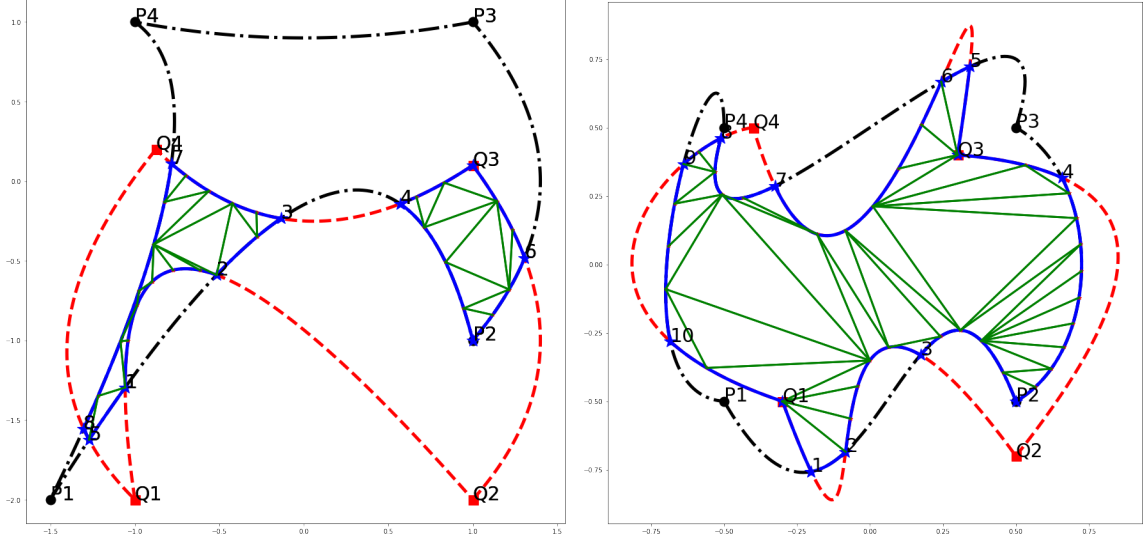


Figure 5.1: Partition of the intersections.

6 The Positivity-preserving modification

When solving fluid dynamics with the ALE method, it is essential to preserve positivity for specific physical variables, such as density and internal energy. This necessitates a remapping method that preserves positivity, which primarily requires ensuring that the integral of the polynomial over the intersection remains positive.

In our curved remapping method, we adopt the same approach as our previous work [18, 19]. If the integral of a polynomial $u_i(x, y)$ over a given intersection is negative $\iint_{\hat{I}_{i,\tilde{i}}} u_i(x, y) dx dy < 0$, we adjust the polynomial based on its values at the quadrature points and the positive cell average \bar{u}_i . Suppose $\hat{I}_{i,\tilde{i}}$ is partitioned into several curved-edge triangles $\hat{I}_{i,\tilde{i}} = \bigcup_{t=1}^T \mathbb{T}_t$, and the quadrature points in \mathbb{T}_t are $\{F_{\mathbb{T}_t}(\xi_m, \eta_m)\}_{m=1}^M$. Define the group of quadrature points in $\hat{I}_{i,\tilde{i}}$ as

$$G(\hat{I}_{i,\tilde{i}}) := \{F_{\mathbb{T}_t}(\xi_m, \eta_m), m = 1, \dots, M, t = 1, \dots, T\},$$

and the set of quadrature points in I_i are $\bigcup_{\tilde{i}=1}^{\tilde{N}} G(\hat{I}_{i,\tilde{i}})$.

Next, we can apply the positivity-preserving limiter in [30], compressing the polynomial

$u_i(x, y)$ towards its positive cell average $\bar{u}_i \geq \varepsilon = 10^{-14}$,

$$\begin{aligned} \hat{u}_i(x, y) &= \theta u_i(x, y) + (1 - \theta)\bar{u}_i, \\ \theta &= \min \left\{ 1, \frac{|\bar{u}_i - \varepsilon|}{|\bar{u}_i - m_i|} \right\}, \quad m_i = \min_{(x,y) \in \bigcup_{i=1}^N G(\hat{I}_{i,\bar{i}})} u_i(x, y), \end{aligned} \quad (6.1)$$

such that the modified polynomial $\hat{u}_i(x, y) \geq \varepsilon > 0$ for all of the quadrature points in I_i . In the meantime, this positivity-preserving modification is also conservative and maintains the original high-order accuracy as proved in [30].

7 Numerical examples

7.1 Accuracy test

Following the methodology of [15, 27], we design a rigorous accuracy verification test for our remapping method. The test configuration employs two distinct curved meshes—the Gresho mesh and the Taylor-Green mesh—initially generated through a pure Lagrangian approach with straight-edge configurations for their respective benchmark problems (Gresho vortex and Taylor-Green flow). To create smooth curvilinear meshes, quadratic curves are subsequently fitted to all grid points derived from the Lagrangian simulation, as illustrated in Figure 7.1. In this test, the Gresho mesh serves as the source domain, while the Taylor-Green mesh acts as the target domain, enabling evaluation of our curved remapping method’s ability to transfer cell averages between them.

We define the remapped physical variable as:

$$u(x, y) = \sin(\pi x) + \sin(\pi y), \quad (x, y) \in [0, 1] \times [0, 1]. \quad (7.1)$$

with its three-dimensional representation on 32×32 Gresho and Taylor-Green meshes visualized in Figure 7.2. The reference solution is established by computing exact cell averages directly on the target mesh, while initial values are derived from cell averages on the source mesh.

To quantify accuracy, we apply our remapping method using first-, third-, and fifth-order WENO reconstructions, denoted as $\bar{u}^{1\text{st}}$, $\bar{u}^{3\text{rd}}$, and $\bar{u}^{5\text{th}}$, respectively. Error metrics are

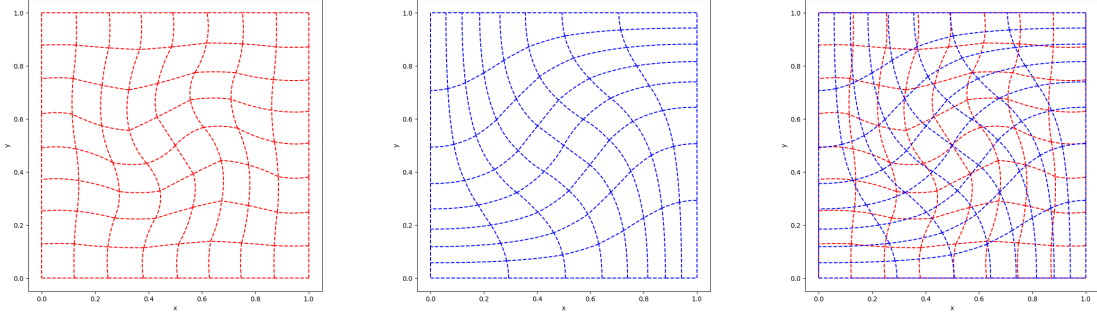


Figure 7.1: Left: Gresho quadratic mesh; Middle: Taylor-Green quadratic mesh; Right: meshes overlapping.

computed by comparing these reconstructed averages against \bar{u}^{ex} , as summarized in Table 7.1. Obviously, our remapping method maintains optimal convergence rates across all tested reconstruction orders, confirming its robustness in practical applications.

In Table 7.2, we show the conservation error of our curved remapping method, where the clipping conservation error e_C^{area} represents the cumulative error between the area of the new curved-edge cell $|\tilde{I}_i|$ calculated using the WA clipping algorithm and the actual area $|\tilde{I}_i^{\text{ex}}|$,

$$e_C^{\text{area}} := \sum_{\tilde{i}=1}^{\tilde{N}} \left| |\tilde{I}_{\tilde{i}}| - |\tilde{I}_{\tilde{i}}^{\text{ex}}| \right|.$$

In the meantime, we define the other three conservation errors for different WENO reconstructions as

$$e_C^{1\text{st}} := \sum_{\tilde{i}=1}^{\tilde{N}} \left| \bar{u}_{\tilde{i}}^{1\text{st}} |\tilde{I}_{\tilde{i}}| - \bar{u}_{\tilde{i}}^{\text{ex}} |\tilde{I}_{\tilde{i}}^{\text{ex}}| \right|, \quad e_C^{3\text{rd}} := \sum_{\tilde{i}=1}^{\tilde{N}} \left| \bar{u}_{\tilde{i}}^{3\text{rd}} |\tilde{I}_{\tilde{i}}| - \bar{u}_{\tilde{i}}^{\text{ex}} |\tilde{I}_{\tilde{i}}^{\text{ex}}| \right|, \quad e_C^{5\text{th}} := \sum_{\tilde{i}=1}^{\tilde{N}} \left| \bar{u}_{\tilde{i}}^{5\text{th}} |\tilde{I}_{\tilde{i}}| - \bar{u}_{\tilde{i}}^{\text{ex}} |\tilde{I}_{\tilde{i}}^{\text{ex}}| \right|.$$

From Table 7.2, we can observe that the clipping error is close to machine zero, and the total conservation error of the three WENO reconstructions are also close to machine zero, which validates that our curved remapping method is conservative.

7.2 The cone test

In this subsection, we consider the following continuous “cone” function,

$$u(x, y) = \begin{cases} 1 - 4r + 10^{-10}, & \sqrt{(x - 0.5)^2 + (y - 0.5)^2} < 0.25, \\ 10^{-10}, & \text{else,} \end{cases} \quad (7.2)$$

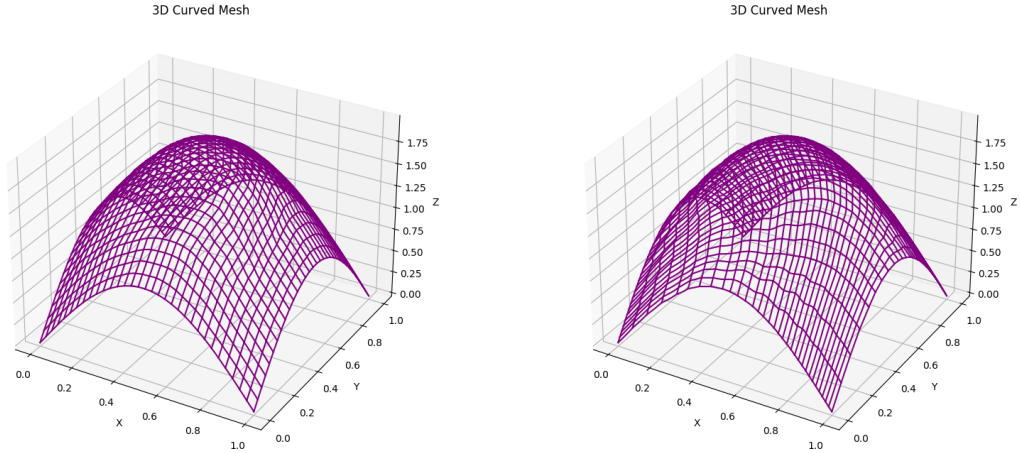


Figure 7.2: Left: the function (7.1) on the source mesh; Right: the function (7.1) on the target mesh.

Table 7.1: Error and order of the remapping results.

Mesh size	L^1 error	order	L^2 error	order	L^∞ error	order
First-order reconstruction $\ \bar{u}^{1st} - \bar{u}^{ex}\ $						
8×8	3.4758E-02		4.3376E-02		1.1057E-01	
16×16	1.3987E-02	1.31	1.8662E-02	1.22	6.4675E-02	0.77
32×32	5.5765E-03	1.33	7.8870E-03	1.24	3.2447E-02	1.00
64×64	2.7064E-03	1.04	3.8512E-03	1.03	1.6289E-02	0.99
Third-order WENO reconstruction $\ \bar{u}^{3rd} - \bar{u}^{ex}\ $						
8×8	1.0244E-03		1.2736E-03		3.1977E-03	
16×16	1.0519E-04	3.28	1.3841E-04	3.20	4.8412E-04	2.72
32×32	1.0762E-05	3.29	1.4833E-05	3.22	6.1104E-05	2.99
64×64	1.3221E-06	3.03	1.8393E-06	3.01	7.6675E-06	2.99
Fifth-order WENO reconstruction $\ \bar{u}^{5th} - \bar{u}^{ex}\ $						
8×8	3.0942E-05		3.7514E-05		9.1281E-05	
16×16	8.3041E-07	5.22	1.0996E-06	5.09	4.0419E-06	4.50
32×32	2.1351E-08	5.28	2.9594E-08	5.22	1.2829E-07	4.98
64×64	6.6991E-10	4.99	9.4255E-10	4.97	4.0452E-09	4.99

Table 7.2: Conservation error of the remapping results.

Mesh size	e_C^{area}	e_C^{1st}	e_C^{3rd}	e_C^{5th}
8×8	9.9920E-16	6.6613E-16	3.5527E-15	3.7748E-15
16×16	4.4409E-16	2.2204E-16	4.6629E-15	7.3275E-15
32×32	1.0103E-14	1.0880E-14	2.4647E-14	1.1524E-13
64×64	2.3204E-14	2.8200E-14	5.5511E-14	1.5699E-13

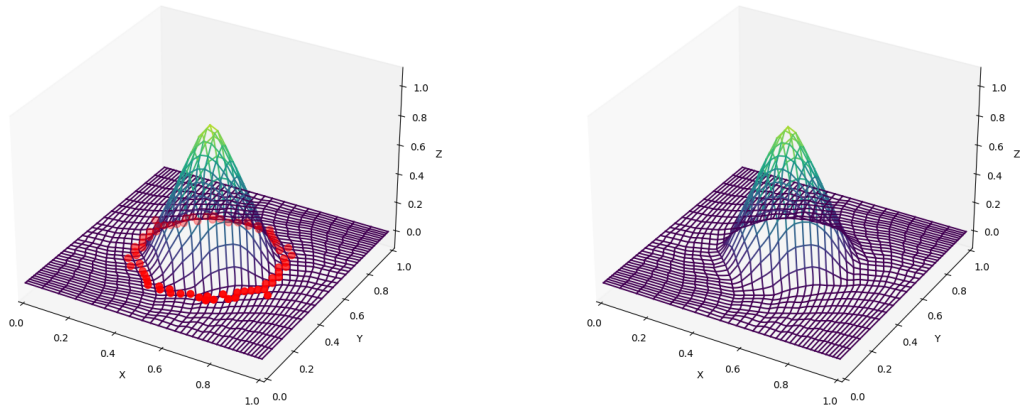


Figure 7.3: The cone test. Left: without the positivity-preserving limiter; Right: with the positivity-preserving limiter. The red markers indicate that the cell averages are negative.

for the positivity-preserving test. As in the previous subsection, we remap the cell averages from the source Gresho mesh to the target Taylor-Green mesh with the third-order WENO reconstruction. We compare the remapping results with or without the positivity-preserving limiter, and we can observe from Figure 7.3 that our limiter preserves positivity well.

7.3 The cylinder test

Next, we remap the cell averages from the source Gresho mesh to the target Taylor-Green mesh with the third-order WENO reconstruction for the following discontinuous “cylinder” function,

$$u(x, y) = \begin{cases} 1, & \sqrt{(x - 0.5)^2 + (y - 0.5)^2} < 0.25, \\ 10^{-10}, & \text{else.} \end{cases} \quad (7.3)$$

We conducted a comparison of the remapping results both with and without the positivity-preserving limiter. Upon examination of Figure 7.4, it is evident that our limiter effectively maintains positivity and that the WENO reconstruction avoids numerical oscillations in the vicinity of discontinuities.

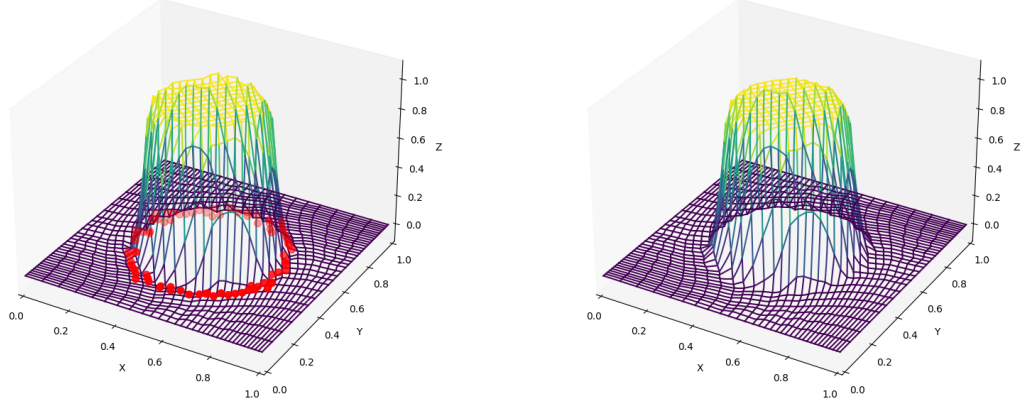


Figure 7.4: The cylinder test. Left: without the positivity-preserving limiter; Right: with the positivity-preserving limiter. The red markers indicate that the cell averages are negative.

7.4 The solid body rotation test

In this part, we consider the test in [1, 21]. The initial function is defined on the unit disk $x^2 + y^2 \leq 1$,

$$u(x, y) = \text{cone}(x, y, \vec{r}_1) + \text{hump}(x, y, \vec{r}_2) + \text{cylinder}(x, y, \vec{r}_3) + 10^{-10},$$

where

$$\begin{aligned}
 \text{cone}(x, y, \vec{r}_1) &= \begin{cases} 0, & \text{otherwise} \\ 1 - r(x, y, \vec{r}_1), & r(x, y, \vec{r}_1) \leq 1 \end{cases} \\
 \text{hump}(x, y, \vec{r}_2) &= \begin{cases} 0, & \text{otherwise} \\ \frac{1}{4}(1 + \cos(\pi r(x, y, \vec{r}_2))), & r(x, y, \vec{r}_2) \leq 1 \end{cases} \\
 \text{cylinder}(x, y, \vec{r}_3) &= \begin{cases} 0, & r(x, y, \vec{r}_3) > 1 \\ 0, & y < 0 \text{ and } |x - \frac{1}{2}| < \frac{0.35}{4} \\ 1, & \text{otherwise} \end{cases}
 \end{aligned} \tag{7.4}$$

with

$$r(x, y, \vec{r}_1) := \frac{1}{0.35} \sqrt{\left(x + \frac{1}{4}\right)^2 + \left(y - \frac{\sqrt{3}}{4}\right)^2},$$

$$r(x, y, \vec{r}_2) := \frac{1}{0.35} \sqrt{\left(x + \frac{1}{4}\right)^2 + \left(y + \frac{\sqrt{3}}{4}\right)^2},$$

$$r(x, y, \vec{r}_3) := \frac{1}{0.35} \sqrt{\left(x - \frac{1}{2}\right)^2 + y^2}.$$

We use Gmsh [13] to generate second-order curvilinear meshes with 3,481 cells. Figure 7.5 displays the two-dimensional and three-dimensional visualizations of $u(x, y)$ evaluated on the initial mesh as well as the mesh subjected to a counterclockwise rotation of $\frac{\pi}{4}$. Notice that, for 3D figures, we only plot the surfaces with cell averages larger than 0.01.

To test our remapping method, we rotate the mesh counterclockwise 2π in increments of $\frac{\pi}{4}$. On each segment of rotation, we apply our curved remapping method described above. In total, we perform 8 remapping times. In Figure 7.6, we show the remapping results after one remapping step and eight remapping steps (returning to the initial mesh), with first-order reconstruction, third-order WENO reconstruction with or without the positivity-preserving limiter. After multiple remapping steps, our remapping method still maintains excellent results, demonstrating the robustness of our method. For the cone function, there is no smearing of the peak, and for the cylinder function, the high-order scheme provides sharper resolution near discontinuities without introducing significant numerical oscillations. Additionally, due to our intersection-based remapping method, we do not need to limit the rotation angle for each remapping step in this case. The rotation of the mesh can be achieved with very few remapping steps, whereas in [21], 40 remapping steps were required (9 degrees per step), and in [1], 1440 remapping steps were needed (1/4 degree per step).

8 Conclusion

In this paper, we present a robust intersection-based remapping method for curvilinear meshes. Utilizing the WA clipping algorithm, our approach efficiently handles cells of arbitrary curvature, even for higher-order or more complex curves, without significantly increasing computational cost. By incorporating high-order numerical integration techniques, multi-

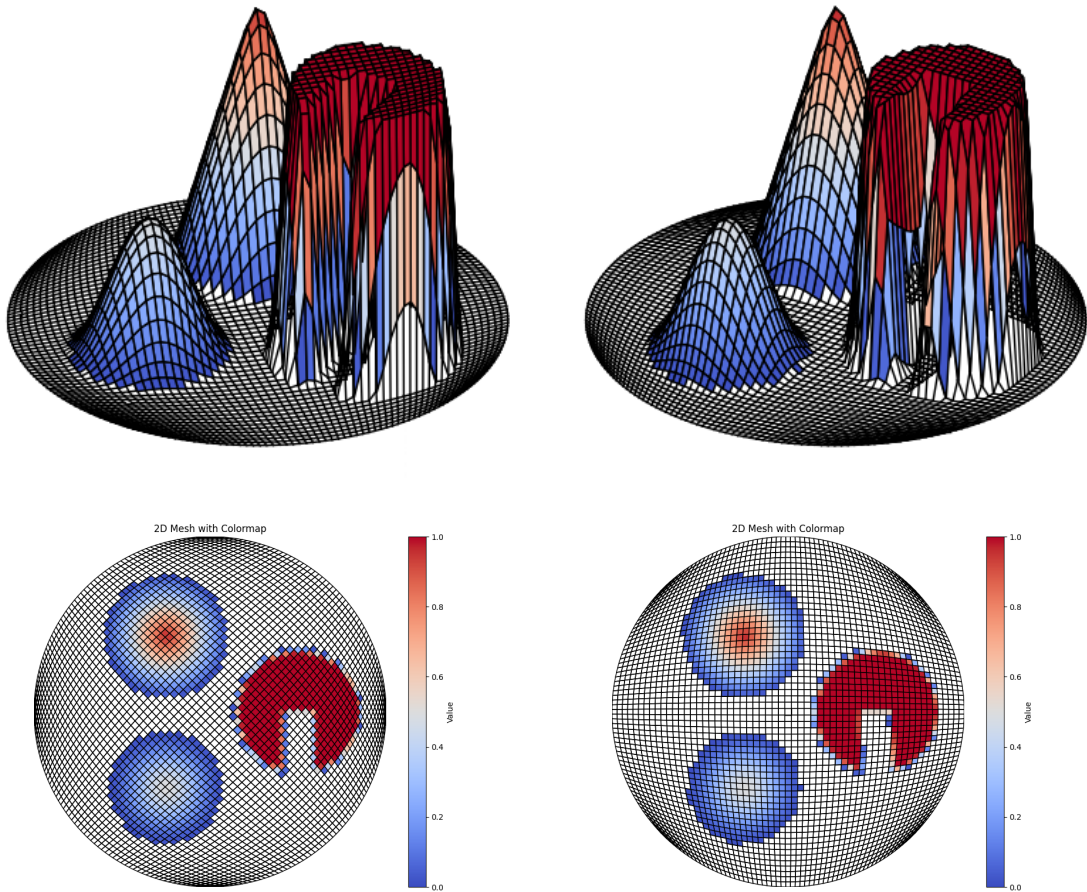


Figure 7.5: The solid body rotation test. Left: Initial function. Right: Rotated $\frac{\pi}{4}$ counter-clockwise.

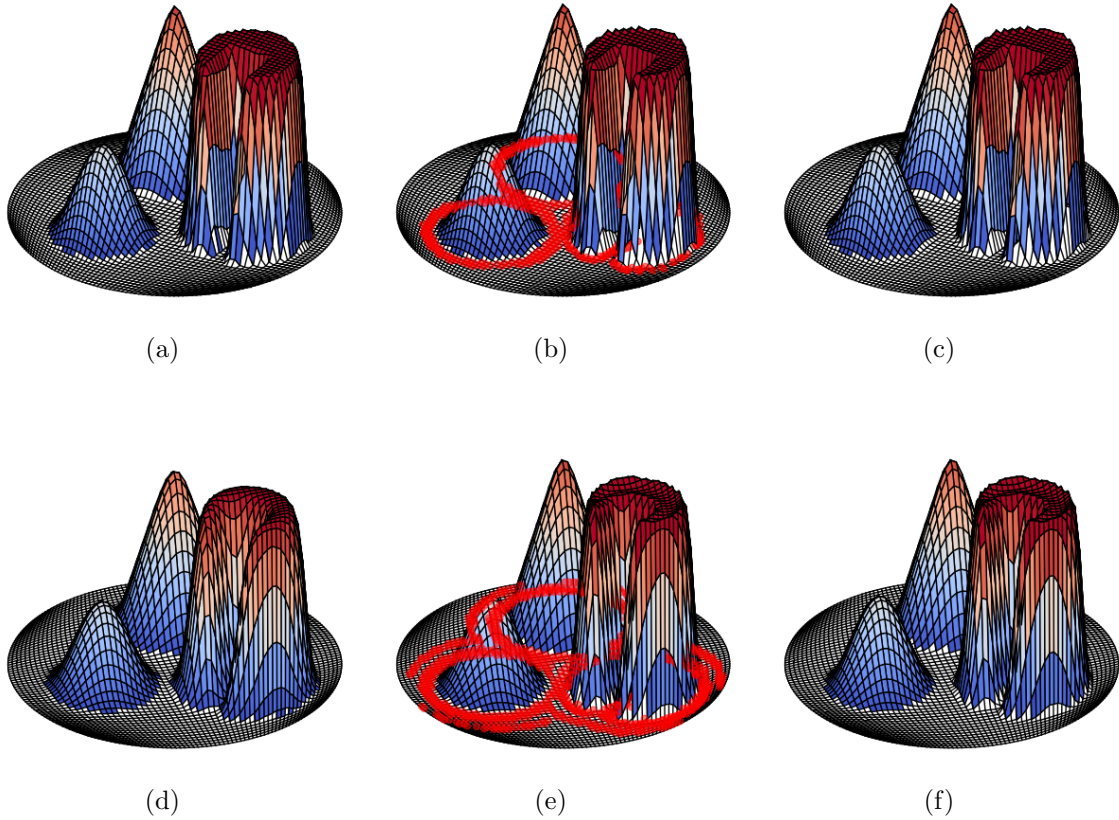


Figure 7.6: The solid body rotation test. Left column: first-order scheme. Middle column: third-order WENO scheme without the positivity-preserving limiter. Right column: third-order WENO scheme with the positivity-preserving limiter. First row: Rotated $\frac{\pi}{4}$ counterclockwise with remapping 1 time. Second row: Rotated 2π counterclockwise with remapping 8 times. The red markers in the left bottom subfigure indicate that the cell averages are negative.

resolution WENO reconstruction, and a positivity-preserving limiter, our method achieves conservation, high-order accuracy, maintains essential non-oscillatory properties, and rigorously preserves positivity without compromising accuracy.

In the future, we aim to first extend this curved remapping method, which is designed for finite volume schemes, to the DG framework. Specifically, we plan to develop high-order, conservative, and positivity-preserving polynomial projection curved remapping method tailored for DG schemes. After that, we aim to develop a high-order curvilinear indirect ALE method, integrating our remapping approach to enhance accuracy and robustness in simulations involving large deformations, complex geometries, and multi-material interactions.

References

- [1] R. W. Anderson, V. A. Dobrev, Tz. V. Kolev, R. N. Rieben, *Monotonicity in high-order curvilinear finite element arbitrary Lagrangian-Eulerian remap*, International Journal for Numerical Methods in Fluids, 77 (2015), 249–273.
- [2] R. W. Anderson, V. A. Dobrev, T. V. Kolev, R. N. Rieben, V. Z. Tomov, *High-order multi-material ALE hydrodynamics*, SIAM Journal on Scientific Computing, 40 (2018), B32–B58.
- [3] A. J. Barlow, P.-H. Maire, W. J. Rider, R. N. Rieben, M. J. Shashkov, *Arbitrary Lagrangian-Eulerian methods for modeling high-speed compressible multimaterial flows*, Journal of Computational Physics, 322 (2016), 603–665.
- [4] G. Blanchard, R. Loubere, *High order accurate conservative remapping scheme on polygonal meshes using a posteriori MOOD limiting*, Computers & Fluids, 136 (2016), 83–103.

- [5] D. E. Burton, N. R. Morgan, M. R. J. Charest, M. A. Kenamond, J. Fung, *Compatible, energy conserving, bounds preserving remap of hydrodynamic fields for an extended ALE scheme*, Journal of Computational Physics, 355 (2018), 492–533.
- [6] J. Cheng, C.-W. Shu, *A high order ENO conservative Lagrangian type scheme for the compressible Euler equations*, Journal of Computational Physics, 227 (2007), 1567–1596.
- [7] J. Cheng, C.-W. Shu, *A third order conservative Lagrangian type scheme on curvilinear meshes for the compressible Euler equations*, Communications in Computational Physics, 4 (2008), 1008–1024.
- [8] L. P. Chew, *Constrained delaunay triangulations*, Algorithmica, 4 (1989), 97–108.
- [9] V. Dobrev, T. Kolev, R. Rieben, *High-order curvilinear finite element methods for Lagrangian hydrodynamics*, SIAM Journal on Scientific Computing, 34 (2012), 606–641.
- [10] J. K. Dukowicz, *Conservative rezoning (remapping) for general quadrilateral meshes*, Journal of Computational Physics, 54 (1984), 411–424.
- [11] J. K. Dukowicz, J. R. Baumgardner, *Incremental remapping as a transport/advection algorithm*, Journal of Computational Physics, 160 (2000), 318–335.
- [12] J. K. Dukowicz, J. W. Kodis, *Accurate conservative remapping (rezoning) for arbitrary Lagrangian-Eulerian computations*, SIAM Journal on Scientific and Statistical Computing, 8 (1987), 305–321.
- [13] C. Geuzaine, J.-F. Remacle, *Gmsh: a three-dimensional finite element mesh generator with built-in pre- and post-processing facilities*, International Journal for Numerical Methods in Engineering, 79 (2009), 1309–1331.
- [14] X. Gu, Y. Li, J. Cheng, C.-W. Shu, *A high order positivity-preserving conservative WENO remapping method based on a moving mesh solver*, Journal of Computational Physics, 473 (2023), 111754.

- [15] M. Kenamond, D. Kuzmin, M. Shashkov, *Intersection-distribution-based remapping between arbitrary meshes for staggered multi-material arbitrary Lagrangian-Eulerian hydrodynamics*, Journal of Computational Physics, 429 (2021), 110014.
- [16] M. Kucharik, M. Shashkov, B. Wendroff, *An efficient linearity-and-bound-preserving remapping method*, Journal of Computational Physics, 188 (2003), 462–471.
- [17] X. Liu, N. R. Morgan, E. J. Lieberman, D. E. Burton, *A fourth-order Lagrangian discontinuous Galerkin method using a hierarchical orthogonal basis on curvilinear grids*, Journal of Computational and Applied Mathematics, 404 (2022), 113890.
- [18] N. Lei, J. Cheng, C.-W. Shu, *A high order positivity-preserving conservative WENO remapping method on 2D quadrilateral meshes*, Computer Methods in Applied Mechanics and Engineering, 373 (2021), 113497.
- [19] N. Lei, J. Cheng, C.-W. Shu, *A high order positivity-preserving polynomial projection remapping method*, Journal of Computational Physics, 474 (2023), 111826.
- [20] E. J. Lieberman, X. Liu, N. R. Morgan, D. J. Luscher, D. E. Burton, *A higher-order Lagrangian discontinuous Galerkin hydrodynamic method for solid dynamics*, Computer Methods in Applied Mechanics and Engineering, 353 (2019), 467–490.
- [21] K. Lipnikov, N. Morgan, *A high-order conservative remap for discontinuous Galerkin schemes on curvilinear polygonal meshes*, Journal of Computational Physics, 399 (2019), 108931.
- [22] K. Lipnikov, N. Morgan, *Conservative high-order discontinuous Galerkin remap scheme on curvilinear polyhedral meshes*, Journal of Computational Physics, 420 (2020), 109712.
- [23] K. Lipnikov, M. Shashkov, *Conservative high-order data transfer method on generalized polygonal meshes*, Journal of Computational Physics, 474 (2023), 111822.

- [24] L. G. Margolin, M. Shashkov, *Second-order sign-preserving conservative interpolation (remapping) on general grids*, Journal of Computational Physics, 184 (2003), 266–298.
- [25] G. H. Meisters, *Polygons have ears*, American Mathematical Monthly, 82 (1975), 648–651.
- [26] D. Powell, T. Abel, *An exact general remeshing scheme applied to physically conservative voxelization*, Journal of Computational Physics, 297 (2015), 340–356.
- [27] M. Shashkov, K. Lipnikov, *Remapping between meshes with isoparametric cells: a case study*, Communications on Applied Mathematics and Computation, 6 (2024), 1551–1574.
- [28] I. Sutherland, G. W. Hodgman, *Reentrant polygon clipping*, Communications of the ACM, 17 (1974), 32–42.
- [29] K. Weiler, P. Atherton, *Hidden surface removal using polygon area sorting*, Computer Graphics, 11 (1977), 214–222.
- [30] X. Zhang, C.-W. Shu, *On maximum-principle-satisfying high order schemes for scalar conservation laws*, Journal of Computational Physics, 229 (2010), 3091–3120.
- [31] J. Zhu, C.-W. Shu, *A new type of multi-resolution WENO schemes with increasingly higher order of accuracy*, Journal of Computational Physics, 375 (2018), 659–683.